Article:
Lekas, S., Drummond, R., Zheng, Q. et al. (2026) Applying feedback control to additive manufacturing of graded refractive index lenses with continuous-distributions in permittivity. Additive Manufacturing, 118. 105089. ISSN: 2214-8604

https://doi.org/10.1016/j.addma.2026.105089

Applying feedback control to additive manufacturing of graded refractive index lenses with continuous-distributions in permittivity

Sophie Lekas[a], Ross Drummond[b], Qianfang Zheng[c], Patrick S. Grant[c], Stephen R. Duncan[a]

[a]*Department of Engineering Science, University of Oxford, Oxford, OX1 3PJ, UK*
[b]*School of Electrical and Electronic Engineering, University of Sheffield, Sheffield, S1 3JD, UK*
[c]*Department of Materials, University of Oxford, Oxford, OX1 3PJ, UK*

Abstract

Graded refractive index (GRIN) lenses focus and direct electromagnetic waves by making use of spatially-varying material properties to achieve compact, low profile devices in a range of technological applications. For microwave applications, GRIN lenses facilitate performance enhancement of key components such as transmitting and receiving horns used in communication devices. However, the fabrication of GRIN lenses with spatially varying permittivity and/or permeability in order to vary the local refractive index is highly challenging. Recently, additive manufacturing has been used to fabricate GRIN lenses with some success, but accurate control of the local refractive index to meet demanding lens designs is difficult. Here, a feedback control system is designed for improved additive manufacturing of GRIN microwave lenses fabricated from a mixture of both polylactic acid (PLA) and an acrylonitrile butadiene styrene/barium titanate (ABS/$BaTiO_3$) composite. After each layer is printed, a controller measures the just-printed

local permittivity distribution using a split ring resonator and automatically updates the composition of the next-to-print layer to ensure the resulting local material properties match the design, thus accounting for any printing inconsistencies or defects. The defect structure of lenses without and with the controller are examined using X-ray tomography, and lens performance assessed in the 12-18 GHz range. Overall, the controller is shown to deliver higher fidelity and performance GRIN lenses by ameliorating print defects in real-time during printing.

---

1. Introduction

Microwaves are the basis for critical telecommunication technologies including mobile phones, radar systems and those used in satellites, and many variants make use of simple microwaves lenses to direct and focus the radiation during both transmission and receiving. Microwave lenses can be bulky (dimensions of many cms) and therefore may also be heavy, making them cumbersome and inefficient to incorporate into compact, lightweight microsystems. Lenses can be reduced in size and weight by use of materials with comparatively high refractive index, and made more conveniently flat and parallel-sided using a spatially varying, or graded refractive index (GRIN). Figure 1 shows (a) a *classical* lens and (b) a *GRIN* lens. For a classical lens, the material properties (e.g. the refractive index η) of the lens are uniform throughout the lens, but the lens has a curved profile. In contrast, GRIN lenses can have the same effect on the incident EM waves, but in this case, by spatially varying the refractive index, they can have flat profiles. Among other benefits, GRIN lenses can also use materials of relatively

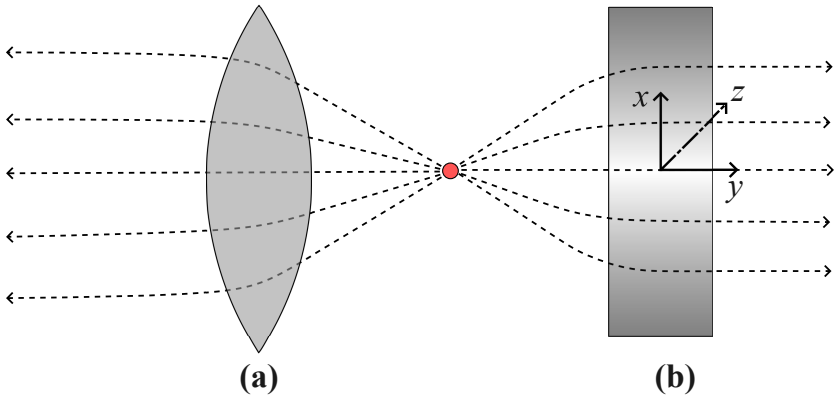

Figure 1: Illustration showing electromagnetic waves being emitted by a source and focused into plane waves by propagating through (a) a classical convex lens and (b) a graded refractive index flat lens. The lens is graded along the x-direction, that is normal to the direction of the incoming waves. This is also the direction the lens is printed, with the material properties remaining constant throughout one layer of deposition.

high refractive index that allow the miniaturisation of several classical devices, including photonic crystals [1], waveguides [2], power splitters [3], and beam collimators [4]. A typical application of GRIN lenses is to boost the gain and directivity of microwave horn antenna, with the lens transforming spherical waves emanating from a focal point into planar waves [5]. These capabilities of GRIN lenses have in turn, supported the development of new meta-material devices, including invisibility cloaks [6, 7], beam splitters [3], wave field concentrators [8], and flat reflectors [9]. The development of these new devices underscores the opportunities of advancing a broad range of technologies through improvements in GRIN lens design.

1.1. Additive manufacturing for GRIN lenses

Constructing GRIN lenses with spatially-varying electromagnetic (EM) properties is a challenging manufacturing problem. One solution [10] introduces a spatially varying array of small, millimetre scale pores or air voids

into the bulk material of the lens by drilling holes into a homogeneous slab to create small variations in local effective permittivity, ϵ_r, which depends upon the proportion of local volume fraction of air ($\epsilon_r = 1$) and lens material ($\epsilon_r > 1$). Changes in the refractive index are achieved because $\eta = \sqrt{\epsilon_r \, \mu_r}$ where μ_r is the relative permeability. Although convenient, drilling has challenges, including: *(i)* requiring precise machining with sub-millimetre accuracy, *(ii)* the number of drilled holes is restricted by the need to maintain structural integrity of the lens, and *(iii)* there is limited, or no, ability to introduce porosity selectively within the interior of the lens.

Recently, greater flexibility of GRIN lens fabrication has been achieved using additive manufacturing (AM). A GRIN lens was fabricated using AM consisting of concentric circles of polylactic acid (PLA), that were printed using the fused filament fabrication (FFF) technique, with each circle having a different local pore fraction, resulting in a spatially varying density [11]. Once again, different fractions of internal air voids changed the local permittivity by varying the local infill density from 100% ($\epsilon_r = 2.72$) at the centre to 10% ($\epsilon_r = 1.30$) at the edge. Alternatively, a flat GRIN lens was printed using two materials of different relative permittivity: one filament of acrylonitrile butadiene styrene (ABS) with $\epsilon_r = 2.6$ and the other a particulate composite consisting of ABS and barium titanate (ABS/$BaTiO_3$) with $\epsilon_r = 7.5$ [12].

While AM may represent a low-cost, flexible and increasingly accessible fabrication technique for GRIN lenses, significant limitations remain. A principal challenge is to reliably and reproducibly achieve the designed spatial variation in local permittivity within the required tolerance. For example,

neither AM lens described above was able to achieve a controlled continuous radial variation in permittivity. This was due to the inability to continuously mix materials within a single layer, because the ideal, smooth radial distribution of permittivity had to be discretised with a step-wise approximation; when the discretisation is relatively coarse to facilitate multi-material printing, the lens became more inhomogeneous and suffered from degraded performance [12]. Similarly, the effectiveness of the lens may also be constrained by the resolution of the printer and how finely each concentric circle could be printed [11]. The ideal smooth variation in permittivity always requires a series of step functions approximated local "zones" of constant permittivity, which may result in significant internal reflection at the interfaces due to the mismatch between the permittivities [13]. Decreasing the discontinuities in permittivity between each "zone" would decrease the strength of these reflected waves and, consequently, enhance antenna gain. Thus, there is interest in fabricating GRIN lenses with continuous spatial variations in permittivity. Even when relatively coarse scale variations are required, there still remains a need to improve the reproducibility of the printed GRIN lens, especially when using high permittivity filaments, which are difficult to print.

1.2. Feedback Control within AM

As described previously, GRIN lenses with spatially-varying electromagnetic properties can be complex to manufacture by AM, and defects are prone to develop during printing. Typical defects include unplanned variations in porosity, imperfect inter-layer bonding, and poor surface finishes; these defects combine to reduce the quality and performance of the lens. For large (mm-scale) internal defects, both the mechanical and electromagnetic

properties of the lens may deteriorate significantly. In AM generally, there is considerable interest in applying feedback control to minimise defects and unplanned local changes in structure and properties, although practical solutions have remained elusive, especially for metallic materials [14]. Here we introduce feedback control during the AM of polymeric based materials to improve the reliability of fabrication and the quality of GRIN lenses by automatically detecting and correcting defects during printing. Most existing controller design studies for AM have focused on regulating process variables, such as laser scan speed, layer thickness etc., to control part quality, including the smoothness of the finish or the accuracy of the layer height. Several different mechanisms have been proposed to implement feedback control in AM, including through changes to the droplet volume [15, 16], the jet frequency of ink-jet printing [17], the temperature of powder bed fusion [18], and the spatial flow rate in laser metal deposition [19]. Recently, data generated during printing has been exploited to improve controller performance; for example, by controlling the extrusion force in FFF [20] and in laser melting [21, 22, 23, 24]. The use of feedback control in FFF has grown in recent years, with several methods now being developed including those that use images [25, 26] and optimise process parameters [27] or geometric properties (e.g. height) [28] on a layer-to-layer basis. In parallel, several control-oriented models have also been developed, including those characterising layer deposition/solidification [29, 30, 31] and designing experiments [32, 33].

While these results show significant progress in controlling the *processes* and *finishes* of printed parts, relatively little attention has been paid to controlling the printed material *properties* directly, which is the key to GRIN

lens performance. The few studies that have focused on controlling spatial properties directly include using model predictive control to regulate the layer width of a fused deposition modelling (FDM) process to meet precise stiffness requirements [34] and proportional-integral-derivative (PID) control to regulate deposition microstructure of metal [35]. In contrast to these results on controlling the *mechanical* properties of printed parts, this paper explores the precise spatial control of the functional, specifically *dielectric*, properties of the printed material.

GRIN lenses manufactured from two filament materials are investigated in this paper: polylactic acid (PLA) and an ABS/$BaTiO_3$ composite (PREPERM, Avient). PLA was chosen as it is low cost and widely used in FFF and ABS/$BaTiO_3$ composite because it is one of only a few commercially available high permittivity materials ($\epsilon_r = 7.5$). The performance of lenses made from these two materials when fitted into a non-optimised short horn microwave antenna are compared, together with the performance of a higher performing, optimised long horn antenna without a lens. Combining a GRIN lens with an otherwise inefficient short horn antenna achieved the same performance as the efficient long horn antenna without a lens, but the lens incorporating the higher permittivity ABS/$BaTiO_3$ lens was 40% smaller. However, the principal finding is that the use of feedback to control the manufacturing of the GRIN lenses improved the microwave performance (gain, directionality) of the assemblies.

2. PRINTING HARDWARE

Figure 2 shows the hardware used to implement feedback control into the additive manufacturing process consisting of three main components: (*i*) an FFF printer [36], (*ii*) a split-ring-resonator sensor (SRR) to measure the permittivity of the deposited material, and (*iii*) a Vector Network Analyser (VNA) that excites and receives measurements from the dielectric sensor. Only an overview of the printing hardware is given here, but further details can be found in [37, 38].

2.1. 3D Printer

The FFF printer was a *ToolChanger and Motion System* (E3D, Oxford, UK) fitted with a Direct Drive Hemera hot-end (V6 0.4 mm Nozzle X, E3D, Oxford, UK).

2.2. Sensor Design

Local permittivity measurements were made during printing using a split-ring-resonator operating in the range 1 to 3 GHz. Fabrication of the split-ring-resonator followed the method described in [39], with two magnetic loops fixed equidistant from a split ring such that they generated an electric field that induced the split ring to resonate at frequency f_0. The two magnetic loops were fabricated using the inner conductor of a Cu semi-rigid coaxial cable (RG402, Farnell, Leeds, UK) that was bent into a loop and then soldered back onto the outer conductor. These two magnetic loops were then held equidistant from the Cu split ring using a 3D-printed case. SMA (Sub-Miniature version A) 50 Ω male connectors were soldered onto the other end

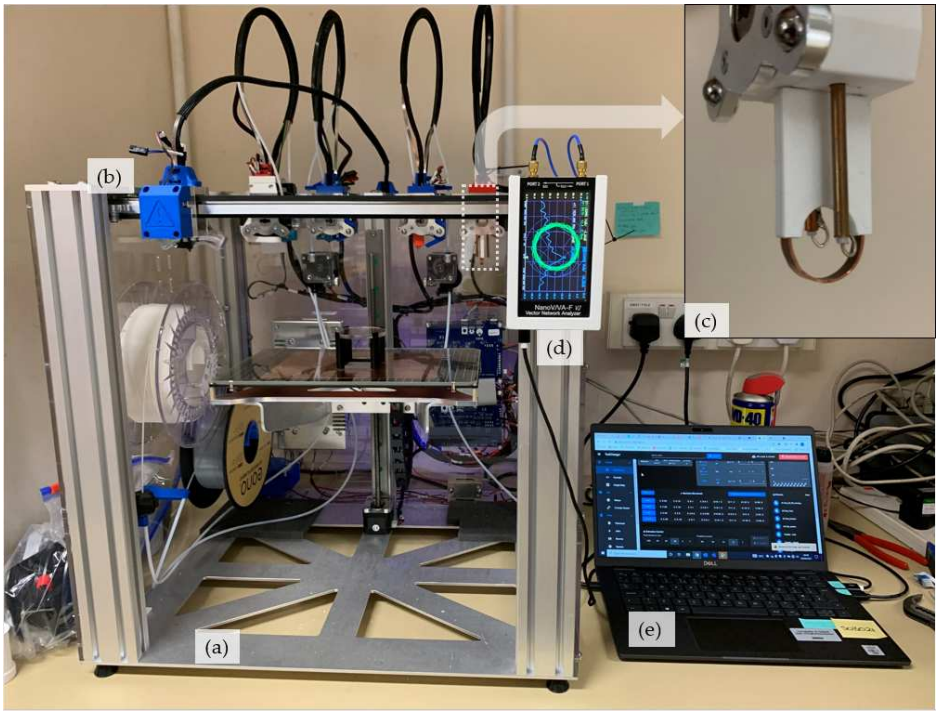

Figure 2: (a) The ToolChanger & Motion System. (b) The ToolHead that selects the print head tool from four options. (c) A SRR device held in a 3D printed case. (d) The VNA attached to the frame. (e) A laptop containing the printing host and running the DuetWebControl UI. See [37] for further details.

of the RG402 cables. Figure 3 shows the SRR taking a measurement during a print.

The resonant frequency of the SRR is shifted by a change in the local dielectric environment in the region of the split in the ring. Using the modelling and experimental results from [40], the shift in the resonant frequency due to the presence of a material, $f_{0,\text{material}}$, compared to that of air, $f_{0,\text{air}}$, depends upon the gap between the SRR and the material,

$$f_{0,\text{material}} = f_{0,\text{air}} - DR \times \exp\left(M_q q^n\right), \tag{1}$$

where q is the gap between the SRR and the material, n and $M_q < 0$ are fitting parameters. DR is the dynamic range which varies with the relative permittivity of the material ϵ_r according to

$$DR = M_e \ln(\epsilon_r), \tag{2}$$

where M_e is a best-fit coefficient depending on the geometry of the SRR. An expression relating the local permittivity of the material near the gap ϵ_r to the shift in the resonant frequency of the SRR $\Delta f_0 = f_{0,\text{air}} - f_{0,\text{material}}$, can then be obtained

$$\epsilon_r = \exp\left(\frac{\Delta f_0}{M_e \exp\left(M_q q^n\right)}\right). \tag{3}$$

Here, $q = 0.2$ mm and $n = 0.1$ were used while the parameters M_e and M_q were fitted using the `greyest` toolbox in MATLAB during the calibration of the SRR at the beginning of each print. During printing, measurements were taken from the geometric centre of the printed surface using the SRR immediately after deposition. This was to make the process as quick as possible. As the extruded polymer cools, it may shrink and change in density and crystallinity over time, which may affect the accuracy of the SRR measurements. Such morphology changes could be sources for the noise seen in the experimental data, e.g. in Figure 10.

2.3. Integrating the VNA

The NanoVNA-F V2 Portable VNA (SYSJOINT, Hangzhou, China) was used to energise the SRR and to measure the resonant frequency f_0. Data transfer was achieved by connecting transfer (TX) and receive (RX) ports to the SRR's RG402 cables with straight 50 Ω SMA-female to SMA-female

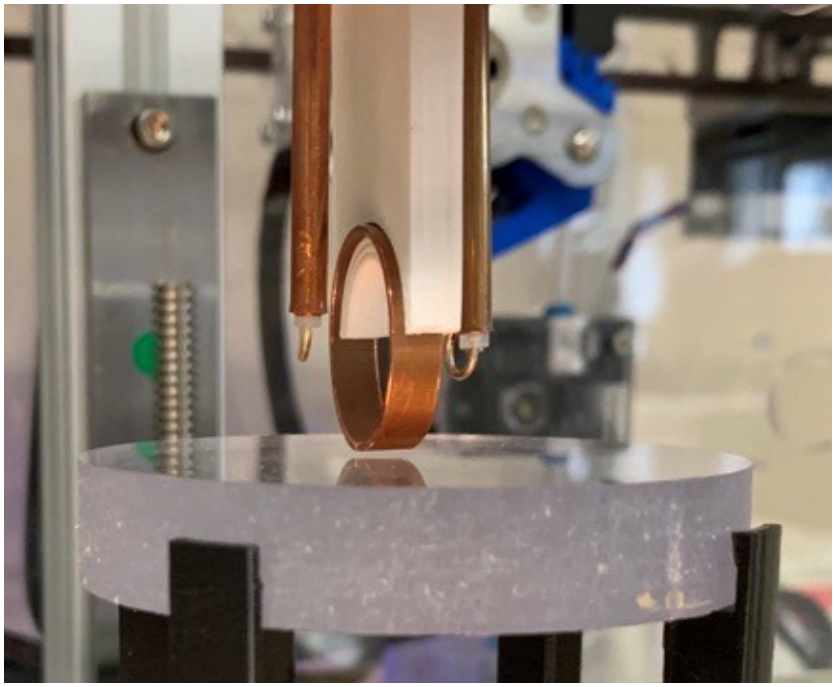

Figure 3: Photograph of the the SRR taking a measurement.

adapters.

3. Material Characterisation of ABS/$BaTiO_3$ Composite

Lenses were fabricated from PLA and an ABS/$BaTiO_3$ composite (PREPERM, Avient) to compare the performance of the control system design for materials that are easy and difficult to print, respectively. For the lens design and control approach, the material properties of the materials must be characterised. For PLA, which is a standard AM material, the characterisation is described in [41, 37]. The following section describes the characterisation of the ABS/$BaTiO_3$ composite.

ABS is a commonly-used material in FFF printing [42], but the addition

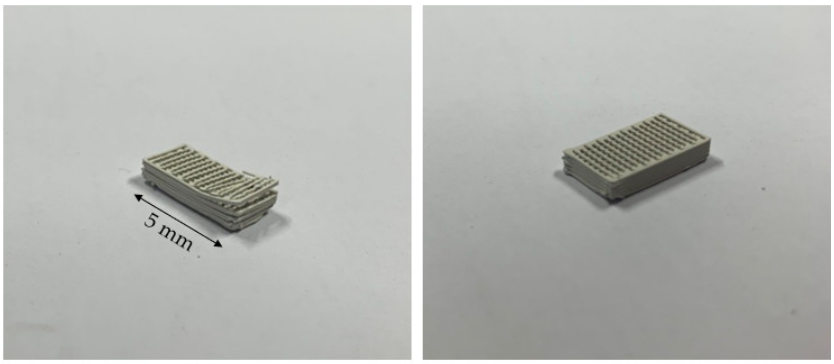

Figure 4: Photographs of a ABS/$BaTiO_3$ sample (a) printed at too low temperature (235 °C) causing poor interlayer adhesion and (b) printed with too high temperature (280 °C) causing over-extrusion buildup at the corners.

of up to 30 vol % $BaTiO_3$ ceramic micro-particles to increase permittivity makes the filament challenging to print, increasing stiffness, roughness and reducing ductility, so that breakage becomes much more likely. As these composites have only recently been produced and are not widely-available commercially, with the exception of [43], there is little research on their optimal print parameters, and any resulting effect on dielectric properties of the printed material.

Temperature. The ABS/$BaTiO_3$ filament was printed on a bed heated to 105°C, slightly above the glass transition temperature [42], to promote adhesion between the print bed and the printed layers. A nozzle temperature between 235 and 280°C was suggested in [42], but the lower end of this range caused layer separation, while the higher end caused over-extrusion at corners, as shown in Figure 4. The optimum printing temperature was found to be 260°C.

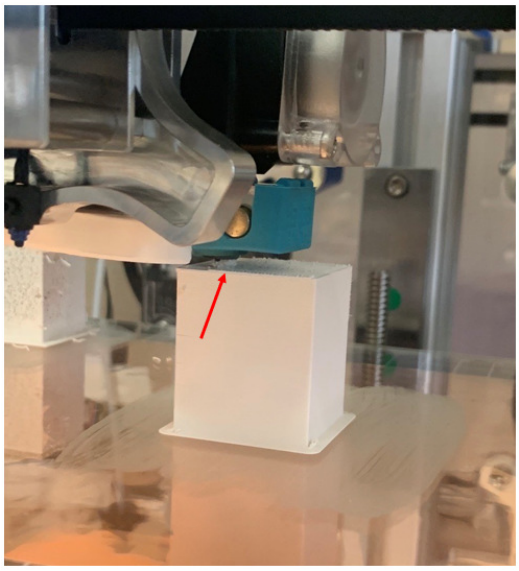

Figure 5: A photograph of the nozzle with excess composite material. The material was not extruded at the correct rate and did not bond with the layer beneath, resulting in printing imperfections because the material stayed in contact with the hot nozzle.

Extrusion Multiplier. This term is common in FFF and is set to ensure a consistent flow of molten material from the hot nozzle. The optimum value to avoid build up at the nozzle (Figure 5) was 1.1.

Printing Speed. The recommended range of print speed was 10–40 mm/s, but gave inconsistent deposition, which was rectified by increasing to a print speed of 70 mm/s.

Infill Density. The higher print speed allowed for an infill density of 15% without loss of edge definition when using a rectilinear print pattern. However, when printing with infill densities above 80%, Figure 6a shows over-extrusion along with an unacceptably rough surface, so that the nozzle and/or the SRR sensor often made contact with deposited material. When the SRR came into contact with the printed surface, the SRR's measurements became

unreliable, as demonstrated in Figure 6c. Therefore, a range of 15–80% infill density was selected for printing the ABS/$BaTiO_3$ composite.

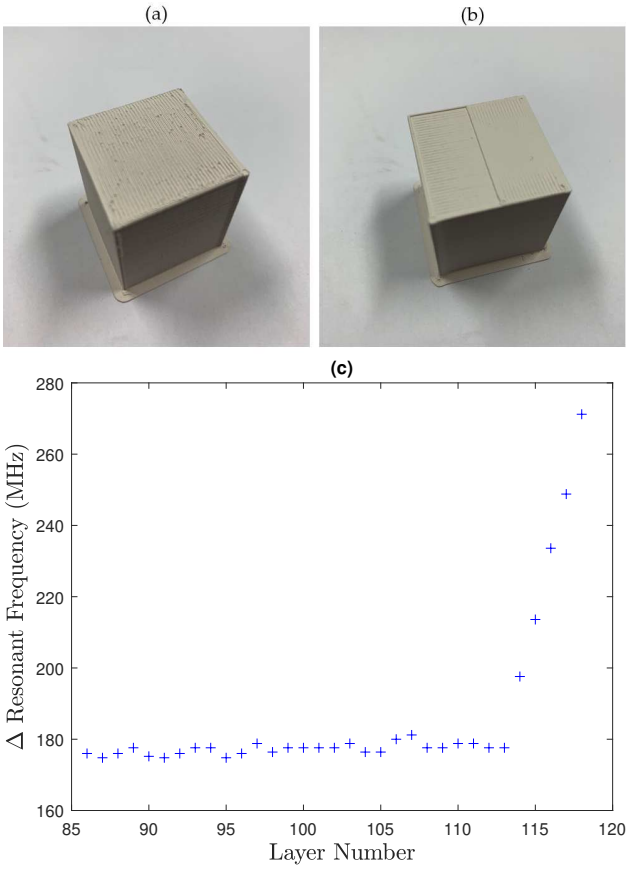

Figure 6: (a) Printed block with top layer printed at 100% infill density. The surface contains areas of raised material and was comparitively rough. (b) Printed block with 80% infill density, halted halfway through a layer to show the normal directions of the rectilinear print pattern. The surface was comparatively smooth. (c) SRR Δf_0 readings of a block printed with a step change from 80% to 100% infill density at layer number 114. At 100% infill, the SRR came into contact with the rough surface, causing a large spike in resonant frequency shift.

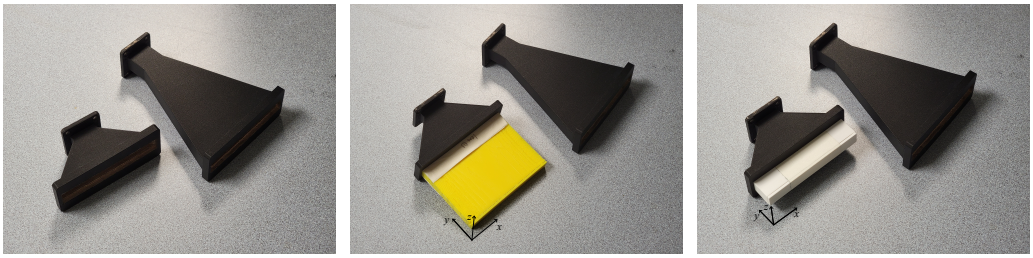

(a) Photograph of the short and long horns.

(b) Photograph of the PLA lens inserted in the short horn.

(c) Photograph of the ABS/$BaTiO_3$ composite lens inserted in the short horn.

Figure 7: The short and long horns used in the experiments. The PLA and ABS/$BaTiO_3$ composite lenses are inserted into the short horns. In each case, the dimensions of the aperture of the microwave horns are width $w = 11$ mm and length $\ell = 84$ mm. The co-ordinate system of the lenses is also shown, with the grading following the printing direction in the x direction.

4. GRIN Lens Design

From the characterisation in [37], printing PLA with a range of 20% to 100% infill density produced a minimum and maximum achievable ϵ_r of 1.17 and 2.98, respectively. To allow the controller to make corrections (as infill densities below 20% or above 100% could not be printed), the lens was designed with a narrow range $\epsilon_{r,\min} = 1.48$ to $\epsilon_{r,\max} = 2.38$. From the characterisation results presented in Figure 8, the minimum and maximum achievable ϵ_r of the ABS/$BaTiO_3$ composite were $\epsilon_{r,\min} = 2$ and $\epsilon_{r,\max} = 7.5$.

At the start of printing, ninety layers were initially printed before a permittivity measurement was taken and the feedback control initiated. This delay was to remove the thermal transient associated with the print bed. Each measurement was a single reading obtained from the geometrical centre of the permittivity-varying zone.

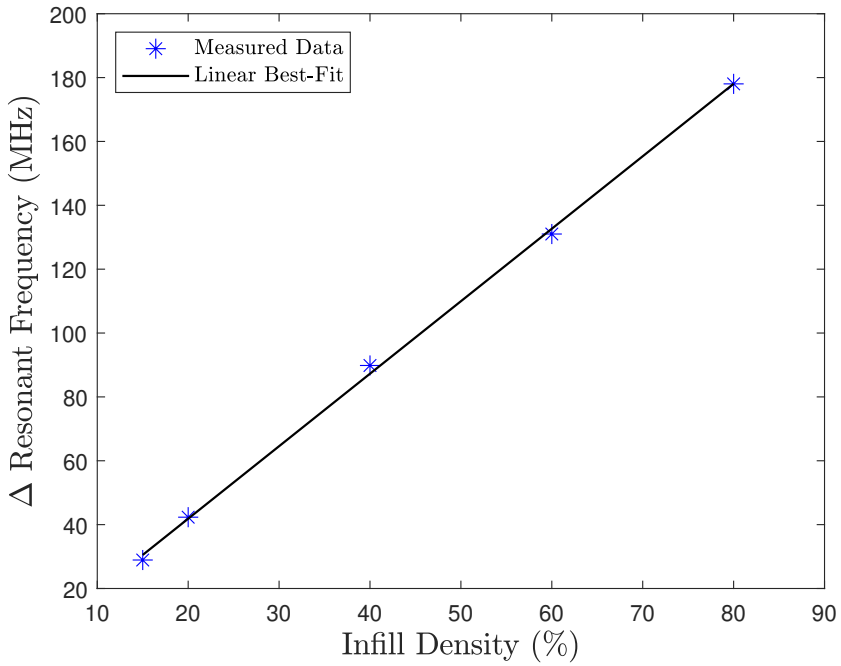

Figure 8: The variation in Δf_0 as a function of printed infill density for ABS/$BaTiO_3$. The line of best fit has an R^2 value of 0.99.

4.1. Spatial distribution of relative permittivity

The dimensions of the GRIN lens were specified to fit into the front aperture of the short microwave horn antennas shown in Figure 7a, with a width of $w = 11$ mm and a length of $\ell = 84$ mm. The spatial distribution of the material properties for the GRIN lens were designed to direct and amplify the EM waves entering the horn antenna from a point source located at a distance d. As for all GRIN lenses, the phase delay of the microwaves exiting the lens was designed to equal that at the centre. Therefore, following the analysis of [12], the permittivity $\epsilon_r(x)$ as a function of distance from the

centre of the lens was distributed according to

$$\epsilon_r(x) = \left(\sqrt{\epsilon_{r,\max}} - \frac{\sqrt{x^2 + d^2} - d}{h} \right)^2, \quad (-\ell/2 \leq x \leq \ell/2) \tag{4}$$

where x is the distance from the centre of the lens, $\epsilon_{r,\max}$ is the maximum refractive index for the printed material at $x = 0$, $\ell = 84$ mm is the length of the lens, $d = 1.5$ m is the distance from the microwave source at the base of the horn and h is the lens height.

Using the values for the maximum and permittivity of both the PLA and ABS/$BaTiO_3$ composite, the height h of the lens was calculated using Equation (4), giving $h = 48.7$ mm and $h = 19.6$ mm respectively, showing the lens size reduction that can be achieved by using higher permittivity materials.

Prior to printing, open-loop sequences for the infill density and permittivity for each layer were obtained with the "*Reference Generator*" block in Figure 9. The reference permittivity was described by Eqn. (4). The reference infill density was generated in two steps: i) using Eqn. (3) to map from the reference permittivity to the reference frequency shift Δf_0 sequence, ii)using the characterisation tests from infill density to frequency shift to get the reference infill density. For the ABS/$BaTiO_3$ composite, Figure 8 describes this infill density-to-frequency shift mapping with the affine equation

$$\Delta f_0 = m(\text{Infill Density}) + b. \tag{5}$$

Parameter values of $m = 2.27$ and $b = -3.54$ were obtained for the ABS/$BaTiO_3$ composite using regression. The parameters values for PLA were $m = 0.986$

and $b = -2.213$ and obtained in [37].

Having calculated the desired profile for $\epsilon_r(x)$ using Equation (4), the corresponding target profile for the spatial variation of the shift in resonant frequency, $\Delta f_0(x)$ can be calculated using (3). As described later, the goal of the feedback control is then to ensure that $\Delta f_0(x)$ follows this target profile as closely as possible while accounting for the impact of any disturbances or defects of the printing process.

The results of Figure 8 show the mapping from infill density to frequency shift Δf_0 for the characterisation tests; in other words from the input (infill density) of the feedback control system to its output (frequency shift). Alternatively, one could plot these results with respect to the physical quantity of permittivity through Eqn. (3). However, this was not done here, as the goal was to use the data of Figure 8 to design the feedback control system. We acknowledge that this may add come confusion to the physical understanding of the results, but believe it simplifies the feedback analysis.

4.2. Impedance matching zones

As the permittivity of the lens is greater than 1, initial lens designs suffered from waves reflection at the various interfaces. To reduce these reflections, two 3mm thick printed impedance-matching layers with $\epsilon_r \sim 2.7$ were added to the front and back flat surfaces of the GRIN lenses. These layers are referred to as the *impedance-matching zones*, and the area between them as the *permittivity-varying zone*.

After printing, the print bed was allowed to cool completely before the print was removed. The initial layers at the start of printing were then removed by machining and the permittivity-varying zone milled to the required

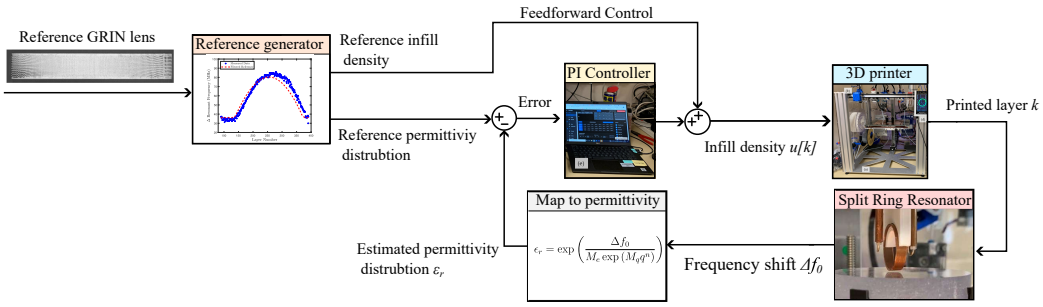

Figure 9: The feedback loop used to the spatial permittivity distributions of the GRIN considered in this paper.

width of 11 mm to fit into the horn.

5. Feedback Control Design

An overview of the feedback control system used in this work can be found in Figure 9. The controller used the printed infill density of the nozzle as the manipulated or actuated variable, while the shift in resonant frequency measured by the SRR was used as the measured variable. This allowed the local infill density to be adjusted to match the required local shift in the resonant frequency. Eqn. (3) was then used to map the shift in resonant frequency to permittivity readings.

However, the shift in resonant frequency at a given layer also depended upon the the frequency shift of the previous printed layer. This meant that the frequency shift $\Delta f_0[k]$ due to the current printed layer can be modelled as a first order response

$$\Delta f_0[k] = c\Delta f_0[k-1] + a\,u[k] + b\,u[k-1], \tag{6}$$

where k denotes the layer number, $u[k]$ is the infill applied at the kth layer,

	a	b	c	k_P	k_I
PLA	0.092	0.092	0.818	1	0.25
ABS composite	0.339	0.339	0.714	0.75	0.25

Table 1: Table containing the model parameters and controller gains for both the PLA and ABS/$BaTiO_3$ composite materials.

and a, b, c are best-fit parameters. To determine the parameters experimentally, a step change of 45% infill density, from 15% to 60% was applied at layer 100 of a print, and the resulting change in SRR resonant frequency at each layer, was recorded, as shown in Figure 10. From these responses, the values of the parameters were estimated by solving regression problems for both PLA and for the ABS/$BaTiO_3$ composite as as shown in Table 1.

It is acknowledged that the first order model of Eqn. (6) is relatively simple, and more accurate predictions could be obtained using more complex dynamics, such as those incorporating non-linearities or hysteresis. However, considering the match to the experimental data of Figure 10 and the previous results of [37], these simple first order dynamics were deemed to be sufficiently accurate for the PI control system design problem considered here. Even though a simple first-order model was used here to design the PI controller, for more complex problems, such as GRIN lens design optimisation, more complex models may be necessary.

5.1. Controller Design

A proportional-plus-integral (PI) controller was designed to provide layer-by-layer feedback control of the part's permittivity during printing following the analysis of [37]. Defining $e[k]$ as the error between the reference permittivity estimated from the SRR and the desired reference value (obtained

from Eqn. (4)), the the controller calculated the required infill density using

$$u[k] = u[k-1] + (k_P + k_I/2)e[k] + (k_I/2 - k_P)e[k-1] \tag{7}$$

where k_p and k_I are the proportional and integral gains of the controller, respectively [37]. The controller gains for the PLA and ABS/$BaTiO_3$ are included in Table 1. The gains were obtained by manual tuning on simulations of the model of (6) using the parameters in Table 1 to achieve reference tracking with limited overshoot [44] and a sufficiently fast error convergence rate. For the PLA, the identified controller gave a stable closed-loop response with an overshoot of 0.8% and a settling time to 2% steady-state error of $k = 13$. For the ABS composite, the controller was also stable, with a overshoot of 0% and a settling time to 2% steady-state error of $k = 6$.

The steps to implement the control action were the following. Immediately after the deposition of a full layer, a SRR measurement was taken from the geometric centre of the printed surface. Then, the infill density to be used for the next layer was calculated from the feedforward reference and the value computed by the feedback controller, which proposes corrections based upon the current SRR measurements. Then, G-code for the next layer was compiled with the new infill density values, and the next layer was printed. This process was then repeated until the end of the print.

6. Results

6.1. PLA

SRR Measurements. GRIN lenses were designed to fit into the short horn antenna as shown in Figure 7b and manufactured from PLA both without

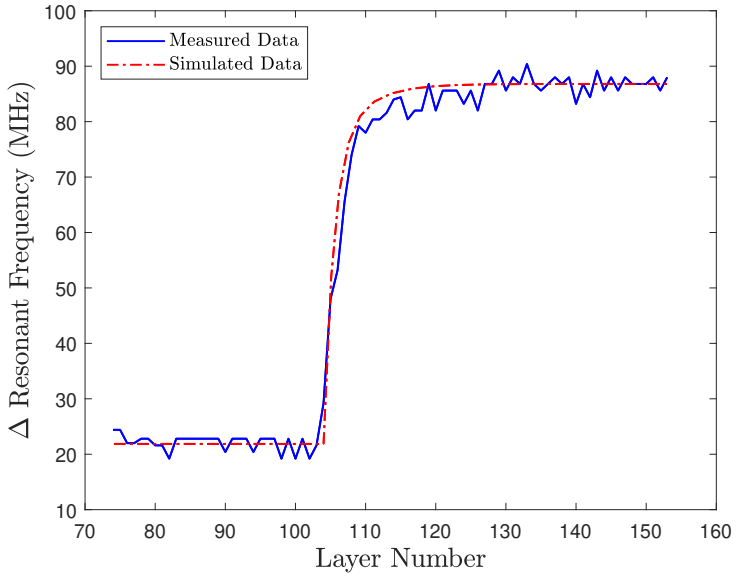

Figure 10: Change in resonant frequency shift due to a step change of 45% infill density at layer 100 for ABS/$BaTiO_3$.

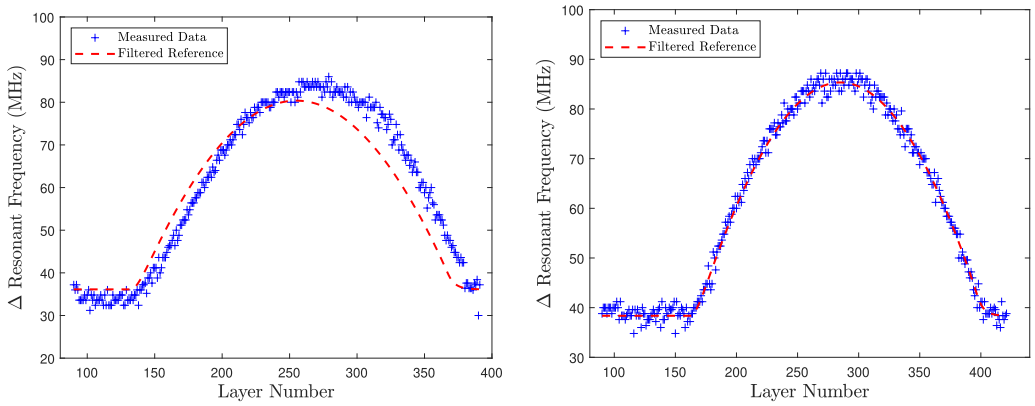

Figure 11: (a) Experimental results of variations in Δf_0 taken during printing of > 400 layers of a the PLA lens using (a) open-loop and (b) closed-loop.

and with feedback control. The corresponding Δf_0 data measured at each layer are plotted in Figure 11, which shows that when closed-loop control was applied, Δf_0 matched the target more closely. In open-loop, the infill

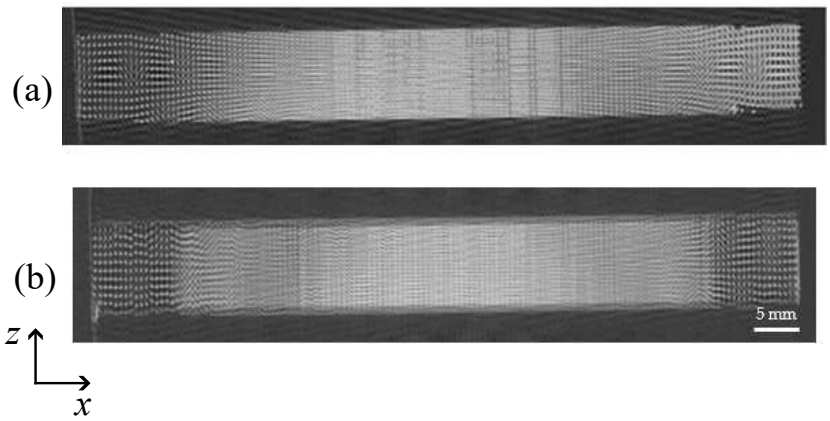

Figure 12: X-ray tomography images of the 3D-printed PLA lenses. (a) xz-plane cut of lens printed open-loop; (b) xz-plane cut of lens printed closed-loop. The pixel resolution of the images are 127×127 microns. See Figure 7 for the orientation of the lens' co-ordinate system in the horns.

densities were too high at the centre of the lens, while in the closed loop lens, the controller accurately regulated the infill changes.

X-Ray Tomography. The internal structure of each lens was investigated using X-ray tomography (ImagiX CT, North Star Imaging Inc., Minnesota, USA), using a X-ray tube with a tungsten target, a tube current of 50 μA, and a tube voltage of 140 kV. The data were reconstructed using efX-CT software (North Star Imaging Inc., Minnesota, USA) and typical 2D slices across the lens are shown in Figure 12. Both lenses show a centre-to-edge decrease in brightness indicating a progressive reduction of infill-density, as intended. However, the lens printed under closed-loop control in Figure 12(b) showed a smoother variation in density and a more symmetric distribution about the centre compared to the lens printed open-loop in Figure 12(a).

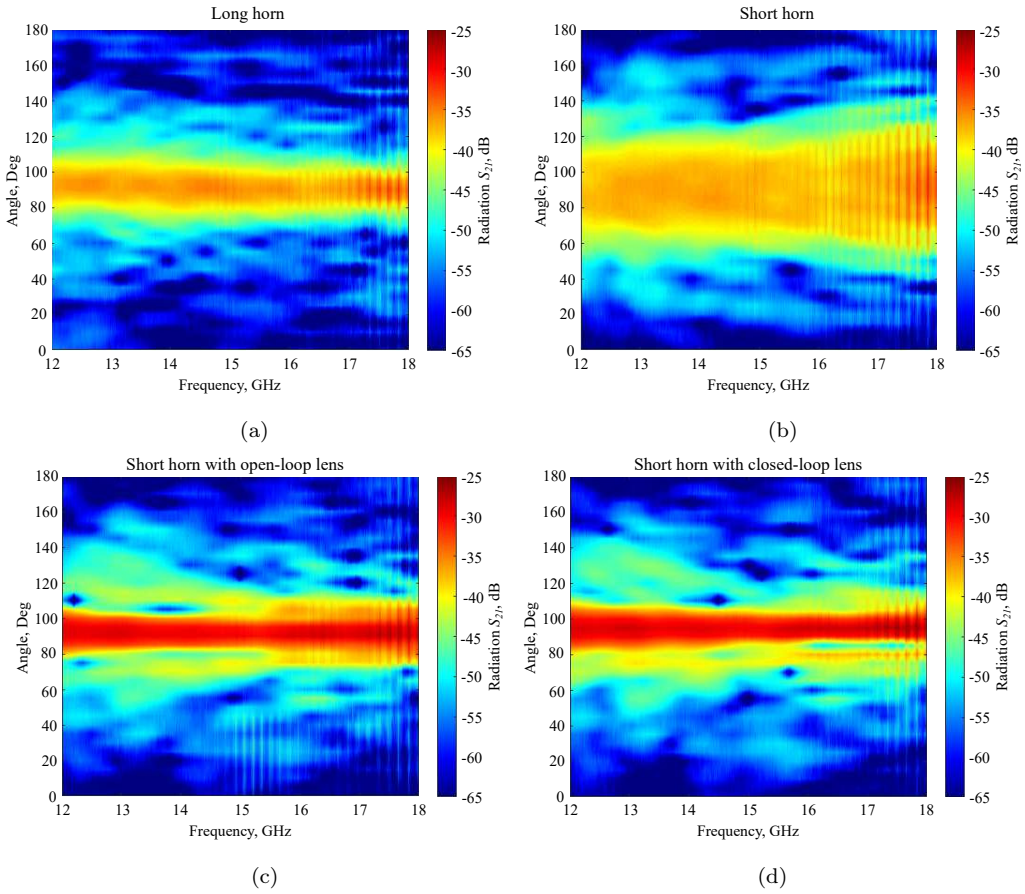

Figure 13: Far-field radiation patterns of (a) the reference long horn, (b) the short horn, (c) the short horn with open-loop PLA lens, and (d) the short horn with closed-loop PLA lens.

Microwave Measurements. The performance of four microwave horn systems were assessed: (*i*) a reference, geometrically optimised longer horn, which was used as a baseline for comparison; (*ii*) a shorter, geometrically inefficient horn without a lens; (*iii*) the short horn coupled with a PLA GRIN lens printed open-loop; and (*iv*) the short horn coupled with a PLA GRIN lens printed closed-loop. Measurements were made in the frequency range 12–18 GHz with the long horn or short horn including a lens used as a transmitter,

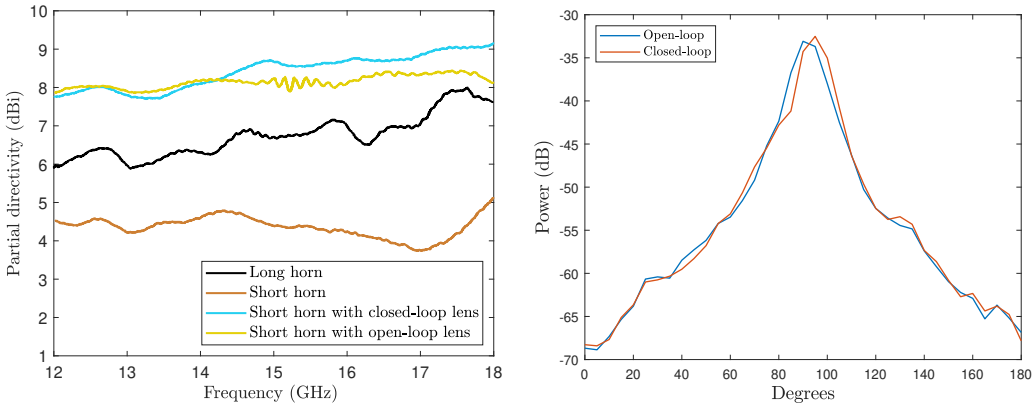

Figure 14: (a) Partial directivity of the four antenna arrangements, including PLA lenses. (b) S_{21} directivity of open-loop and closed-loop lenses

and a standard pyramid waveguide horn antenna at a distance of d =1.5 m along the lens axis used as the receiver. The transmitter was rotated from $-90°$ to $+90°$ in 5° increments and the received signal strength recorded. The whole arrangement was placed in an anechoic chamber. The resulting far-field radiation patterns are presented in Figures 13 (a) to (d), and the directionality plotted as a function of frequency in Figure 14(a). As expected from [12], the optimized reference horn and the short horn with either GRIN lens were significantly more directive than the short horn alone and the open-loop and closed-loop lenses showed broadly similar directivity. However, at 16-18 GHz, the closed-loop lens begins to outperform the open-loop lens by up to 7%. Figure 14(b) shows the calculated focussed power of the two GRIN lens systems and the half-power beamwidth (HPBW) of both antennas was in the range of 10–12°, and they had side lobes at 50° and 130° below -50 dB (Figure 14b).

The return loss behaviour, measured from the S_{11} signal, of both lenses

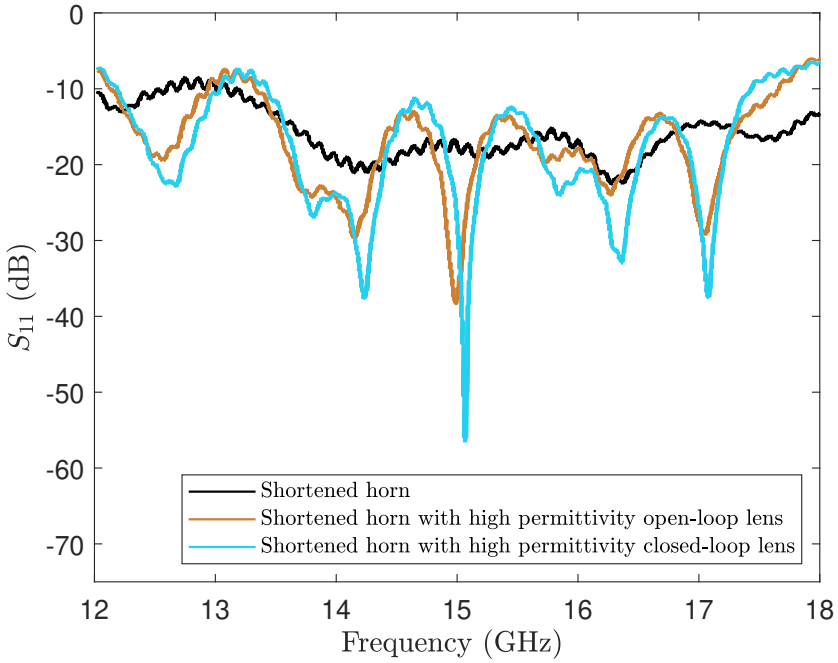

Figure 15: S_{11} measurements of the return loss of the short horn with both open- and closed-loop PLA lenses.

is shown in Figure 15. While the closed-loop lens performed slightly better, they both show a return loss below -12 dB, indicating the effectiveness of the impedance-matching layers in minimising reflection.

6.2. ABS/$BaTiO_3$ composite

SRR Measurements. Figure 16 shows the variation of the reference target and the measured Δf_0 as a function of layer number during the printing of the ABS/$BaTiO_3$ GRIN lens without and with closed-loop control, respectively. Initially, the target and actual Δf_0 closely agreed, but after the mid-point of the lens, the measured frequency shift in the open-loop case began to deviate and the error became progressively larger. In contrast, when printing the lens under closed-loop control, the closed-loop controller automatically adjusted

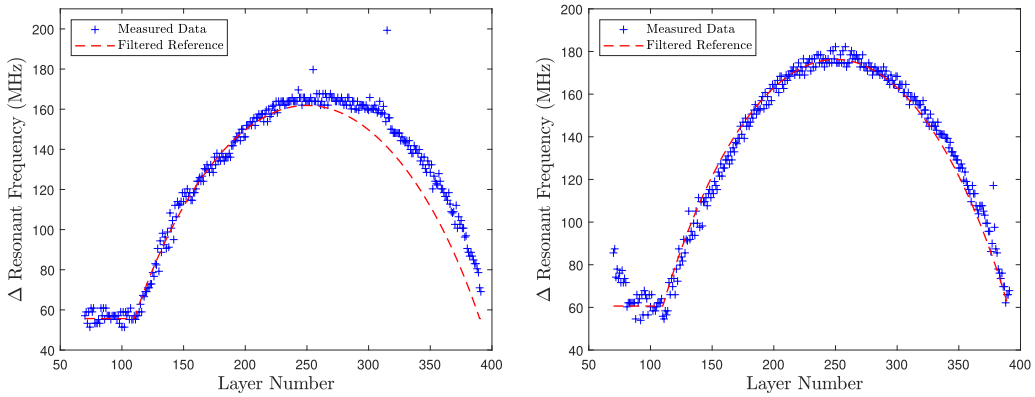

Figure 16: Experimental results of Δf_0 taken during printing of the ABS/$BaTiO_3$ lens for (a) open-loop and (b) closed-loop.

for any similar perturbation in real-time and the measured and target plots remained closely matched.

X-Ray Tomography. As previously, X-ray tomography was used to investigate the lenses and 2D slices of the open- and closed-loop cases are shown in Figure 17. Once again, the closed-loop lens showed much better infill density symmetrty around the centre-line, which was a direct consequence of the frequency shift matching the required target profile, as shown in Figure 16(b).

Microwave Measurements. The performance of the open- and closed-loop lenses were investigated when attached to the short horn antenna. As in the case of the PLA lens, the arrangements were investigated in the 12–18 GHz frequency range. The far-field radiation patterns in Figure 18 (a) and (b) of the open- and closed-loop lenses with the short horn shows that the performance of the lenses was similar, which was confirmed by the directivity

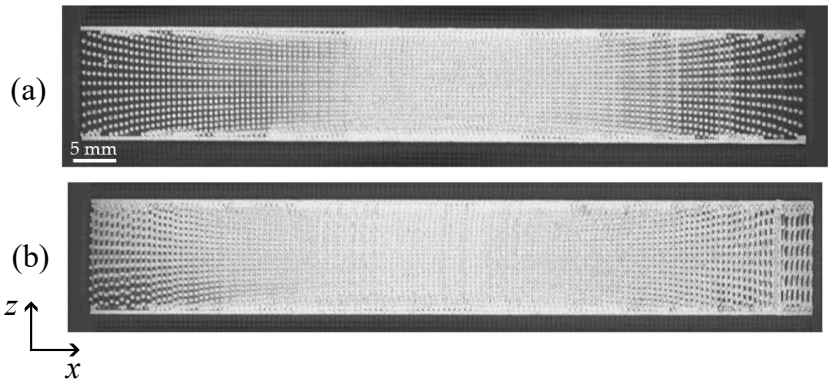

Figure 17: X-ray tomography images of 3D-printed ABS composite lenses. (a) xz-plane cut of lens printed open-loop. (b) xz-plane cut of lens printed closed-loop. The pixel resolution of the images are 127×127 microns. See Figure 7 for the orientation of the lens' co-ordinate system in the horns.

plots as a function of frequency in Figure 19. The similarity in performance between the open- and closed-loop ABS/$BaTiO_3$ composite lenses was a result of the PREPERM filament being fundamentally more challenging to print than PLA. Because of these printing difficulties, careful tuning of the set-up had to be implemented to successfully print an open-loop lens. The tuned set-up meant that only minor defects remained in the open-loop lens, as larger defects would have caused a total failure. There was then only a limited opportunity for the closed-loop system to deliver further gains. The role of the controller for printing with the ABS/$BaTiO_3$ composite was then instead to ensure the lens symmetry consistent with the design. The half power beam width (HPBW) of both antennas was in the range of 5–10°, an improvement upon the HBPW of the PLA lens in the 10-15° range. Both antennas had side lobes at 60° and 120° below -50 dB. The similar return loss behaviour for the lenses is shown in Figure 20.

The advantages of closed-loop printing with challenging materials (such

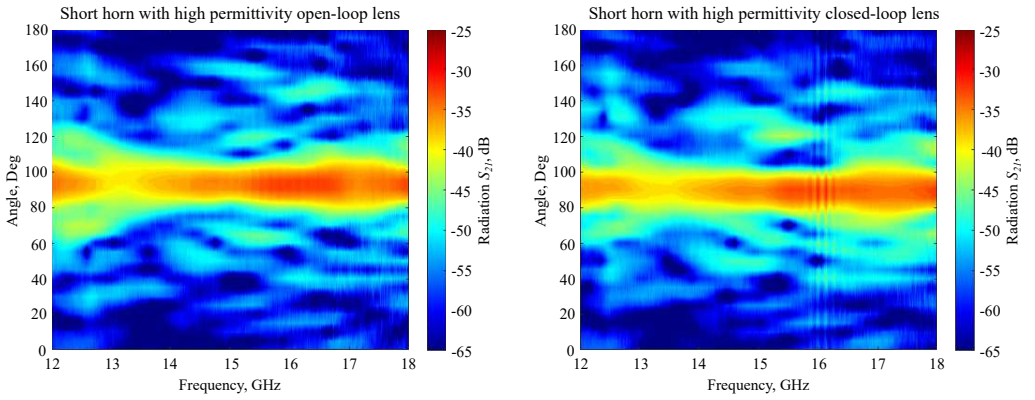

(a) (b)

Figure 18: Far-field radiation patterns of (a) short horn with open-loop ABS/$BaTiO_3$ composite lens and (b) short horn with closed-loop ABS/$BaTiO_3$ composite lens.

as the ABS/$BaTiO_3$ composite) are expected to be more noticeable when fabricating GRIN lenses with complex two- or three-dimensional spatially varying dielectric distributions, such as Eaton [45] or Luneburg lenses [46]. As both the geometric and material complexity increases, the risk of printing defects rises, and the requirement for precise control over local electromagnetic properties becomes more critical. In such cases, closed-loop control with real-time, layer-by-layer monitoring of permittivity could enable the dynamic adjustment of infill density to meet the designed properties more accurately. Early detection of process drift or nozzle blockages could also be implemented. By working in closed-loop, the need for extensive manual tuning would be reduced, print reliability would be improved, material waste would be less, and and there would be lower performance degradation from structural defects or deviations from the intended local permittivity. All of these issues highlight the potential of closed-loop control for printing components with complex functional material property distributions.

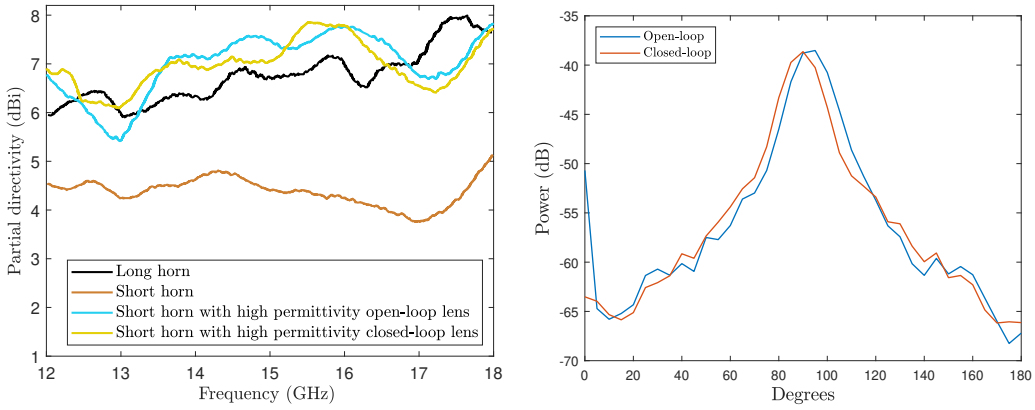

(a) (b)

Figure 19: (a) S_{21} directivity of both an open- and closed-loop ABS/$BaTiO_3$ composite lens. (b) Partial directivity of the open- and closed-loop ABS/$BaTiO_3$ composite lenses.

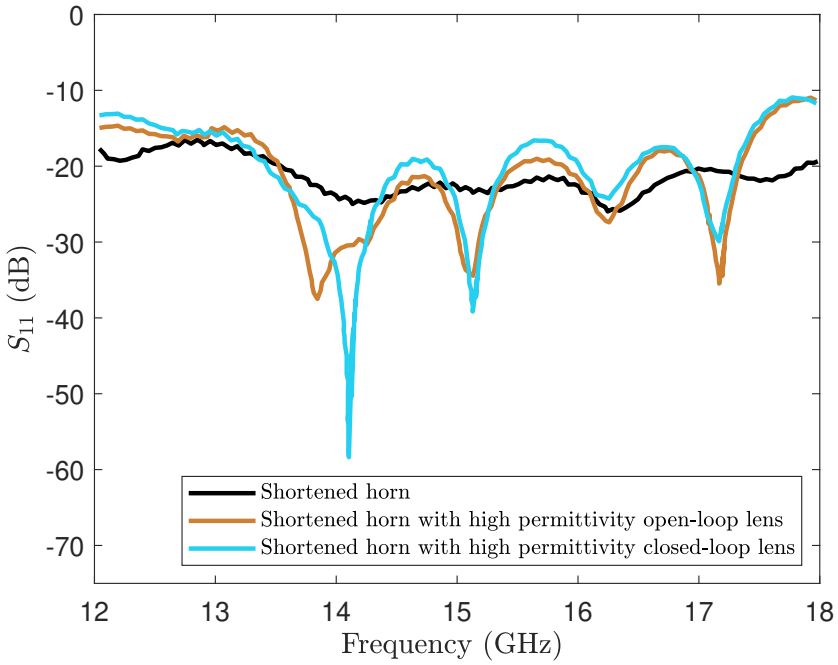

Figure 20: S_{11} measurements of the return loss of the short horn with both an open- and closed-loop ABS/$BaTiO_3$ composite lens.

7. Conclusions

The design and implementation of a feedback control system for additive manufacture of graded refractive index (GRIN) lenses has been demon-

strated. The control system used a split ring resonator to measure the local permittivity of the just-printed material during printing and a tuned proportional-integral controller provided corrective action by varying the local infill density of the next-to-print layer to ensure that the average local material properties followed a designed permittivity profile. The control system was used to manufacture GRIN lenses using PLA, which has a relatively low permittivity of 2.7, but is widely available, and an ABS polymer containing $BaTiO_3$ particulate, which has higher permittivity of 7.5. Although it was more difficult to manufacture GRIN lenses using an ABS/$BaTiO_3$ composite due to its lack of ductility, the key benefit of using a material with high permittivity was that the lens dimensions could be reduced. The control system was able to automatically identify defects during the print process and to apply corrective action in real-time to mitigate them. GRIN lenses made under closed loop control tracked the designed permittivity spatial profile more accurately. The quality of the printed lenses was investigated using X-ray tomography and showed that manufacturing under closed loop control gave a more symmetric and closer to design distribution of local density. The performance of the lenses was also evaluated in the frequency range 12-18 GHz and the closed-loop PLA lens had higher directivity than the open-loop lens. For the ABS/$BaTiO_3$ lens, the open- and closed-loop lenses performed similarly, in part because small local permittivity errors had a reduced impact on the performance of the higher permittivity ABS/$BaTiO_3$ lens. An extension of the feedback control system would involve the SRR tracking behind the print head rather than taking a measurement at the end of each complete layer, which would have the advantage that spatial control of per-

mittivity could then be applied across the plane of the part, rather than between layers, giving full 3D control of the fabrication process. Future work could also explore the application of feedback control to generate more complex graded index lenses than those considered here, for example those whose permittivity varies in all three spatial dimensions. Finally, whilst the x-ray tomography results of Section 6 provide qualitative metrics on the benefits of feedback control for printing GRIN lenses, the use of more quantifiable metrics (e.g. porosity volume fractions or size distributions) would provide further insight. Although exemplified here for the particular AM case of FFF polymer and composite filaments for microwave components, the work more broadly demonstrates a successful realisation of closed-loop control in AM based on material properties, rather than control of print parameters.

References

[1] R. C. Rumpf, J. Pazos, C. R. Garcia, L. Ochoa, R. Wicker, 3D printed lattices with spatially variant self-collimation, Progress In Electromagnetics Research 139 (2013) 1–14.

[2] D. A. Roberts, M. Rahm, J. B. Pendry, D. R. Smith, Transformation-optical design of sharp waveguide bends and corners, Applied Physics Letters 93 (25) (2008) 251111.

[3] D.-H. Kwon, D. H. Werner, Polarization splitter and polarization rotator designs based on transformation optics, Optics Express 16 (23) (2008) 18731–18738.

[4] D.-H. Kwon, D. H. Werner, Transformation optical designs for wave

collimators, flat lenses and right-angle bends, New Journal of Physics 10 (11) (2008) 115023.

[5] J. Suszek, A. Siemion, M. S. Bieda, N. Błocki, D. Coquillat, G. Cywiński, E. Czerwińska, M. Doch, A. Kowalczyk, N. Palka, et al., 3-D-printed flat optics for THz linear scanners, IEEE Transactions on Terahertz Science and Technology 5 (2) (2015) 314–316.

[6] H. Chen, C. Chan, P. Sheng, Transformation optics and metamaterials, Nat. Mater 9 (5) (2010) 387–396.

[7] W. Cai, U. K. Chettiar, A. V. Kildishev, V. M. Shalaev, Optical cloaking with metamaterials, Nature Photonics 1 (4) (2007) 224–227.

[8] M. Sadeghi, S. Li, L. Xu, B. Hou, H. Chen, Transformation optics with Fabry-Pérot resonances, Scientific Reports 5 (1) (2015) 1–7.

[9] W. Tang, C. Argyropoulos, E. Kallos, W. Song, Y. Hao, Discrete coordinate transformation for designing all-dielectric flat antennas, IEEE Transactions on Antennas and Propagation 58 (12) (2010) 3795–3804.

[10] A. Petosa, A. Ittipiboon, Design and performance of a perforated dielectric Fresnel lens, IEE Proceedings-Microwaves, Antennas and Propagation 150 (5) (2003) 309–314.

[11] S. Zhang, R. K. Arya, S. Pandey, Y. Vardaxoglou, W. Whittow, R. Mittra, 3D-printed planar graded index lenses, IET Microwaves, Antennas & Propagation 10 (13) (2016) 1411–1419.

[12] D. Isakov, C. J. Stevens, F. Castles, P. S. Grant, 3D-printed high dielectric contrast gradient index flat lens for a directive antenna with reduced dimensions, Advanced Materials Technologies 1 (6) (2016) 1600072.

[13] P. Russell, Optics of Floquet-Bloch waves in dielectric gratings, Applied Physics B 39 (4) (1986) 231–246.

[14] H. Lhachemi, A. Malik, R. Shorten, Augmented reality, cyber-physical systems, and feedback control for additive manufacturing: A review, IEEE Access 7 (2019) 50119–50135.

[15] P. Ben-Tzvi, R. B. Mrad, A. A. Goldenberg, A conceptual design and FE analysis of a piezoceramic actuated dispensing system for microdrops generation in microarray applications, Mechatronics 17 (1) (2007) 1–13.

[16] L. Lu, J. Zheng, S. Mishra, A layer-to-layer model and feedback control of ink-jet 3-D printing, IEEE/ASME Transactions on Mechatronics 20 (3) (2014) 1056–1068.

[17] K. Barton, S. Mishra, A. Alleyne, P. Ferreira, J. Rogers, Control of high-resolution electrohydrodynamic jet printing, Control Engineering Practice 19 (11) (2011) 1266–1273.

[18] Q. Zhong, X. Tian, X. Huang, C. Huo, D. Li, Using feedback control of thermal history to improve quality consistency of parts fabricated via large-scale powder bed fusion, Additive Manufacturing 42 (2021) 101986.

[19] P. M. Sammons, M. L. Gegel, D. A. Bristow, R. G. Landers, Repetitive process control of additive manufacturing with application to laser metal

deposition, IEEE Transactions on Control Systems Technology 27 (2) (2018) 566–575.

[20] X. Guidetti, A. Mukne, M. Rueppel, Y. Nagel, E. C. Balta, J. Lygeros, Data-driven extrusion force control tuning for 3D printing, arXiv preprint arXiv:2403.16470 (2024).

[21] D. Liao-McPherson, E. C. Balta, R. Wüest, A. Rupenyan, J. Lygeros, In-layer thermal control of a multi-layer selective laser melting process, in: Procs. of the European Control Conference (ECC), IEEE, 2022, pp. 1678–1683.

[22] R. Zuliani, E. C. Balta, A. Rupenyan, J. Lygeros, Batch model predictive control for selective laser melting, in: Procs. of the European Control Conference (ECC), IEEE, 2022, pp. 1560–1565.

[23] B. Kavas, E. C. Balta, M. Tucker, A. Rupenyan, J. Lygeros, M. Bambach, Layer-to-layer closed-loop feedback control application for inter-layer temperature stabilization in laser powder bed fusion, Additive Manufacturing 78 (2023) 103847.

[24] D. Liao-McPherson, E. C. Balta, M. Afrasiabi, A. Rupenyan, M. Bambach, J. Lygeros, Layer-to-layer melt pool control in laser powder bed fusion, IEEE Transactions on Control Systems Technology (2024).

[25] M. Moretti, A. Rossi, In-process monitoring of part geometry in fused filament fabrication using computer vision and digital twins, Additive Manufacturing 37 (2021) 101609.

[26] Y. Lin, X. Guidetti, Y. Nagel, E. C. Balta, J. Lygeros, One-shot camera-based extrusion optimization for high speed fused filament fabrication, arXiv preprint arXiv:2512.24905 (2025).

[27] P. Nath, J. D. Olson, S. Mahadevan, Y.-T. T. Lee, Optimization of fused filament fabrication process parameters under uncertainty to maximize part geometry accuracy, Additive manufacturing 35 (2020) 101331.

[28] E. C. Balta, D. M. Tilbury, K. Barton, Iterative learning spatial height control for layerwise processes, Automatica 167 (2024) 111756.

[29] E. C. Balta, D. M. Tilbury, K. Barton, Layer-to-layer stability of linear layerwise spatially varying systems: Applications in fused deposition modeling, IEEE Transactions on Control Systems Technology 29 (6) (2021) 2517–2532.

[30] S. Koga, M. Krstic, J. Beaman, Laser sintering control for metal additive manufacturing by PDE backstepping, IEEE Transactions on Control Systems Technology 28 (5) (2020) 1928–1939.

[31] P. Hagqvist, A. Heralić, A.-K. Christiansson, B. Lennartson, Resistance based iterative learning control of additive manufacturing with wire, Mechatronics 31 (2015) 116–123.

[32] Y. Guo, J. Peters, T. Oomen, S. Mishra, Control-oriented models for ink-jet 3D printing, Mechatronics 56 (2018) 211–219.

[33] D. Drotman, M. Diagne, R. Bitmead, M. Krstic, Control-oriented energy-based modeling of a screw extruder used for 3D printing, in: Pro-

ceedings ASME Dynamic Systems and Control Conference, Minneapolis, MN, 2016, p. V002T21A002.

[34] K. Garanger, T. Khamvilai, E. Feron, Validating feedback control to meet stiffness requirements in additive manufacturing, IEEE Transactions on Control Systems Technology 28 (5) (2020) 2053–2060.

[35] M. H. Farshidianfar, A. Khajepour, A. Gerlich, Real-time control of microstructure in laser additive manufacturing, The International Journal of Advanced Manufacturing Technology 82 (5-8) (2016) 1173–1186.

[36] D. V. Isakov, Q. Lei, F. Castles, C. Stevens, C. Grovenor, P. Grant, 3D printed anisotropic dielectric composite with meta-material features, Materials & Design 93 (2016) 423–430.

[37] S. Lekas, R. Drummond, P. S. Grant, S. R. Duncan, Control of additive manufacturing for radio frequency devices with spatially varying dielectric properties, IEEE Transactions on Control Systems Technology 32 (5) (2024) 1579–1589.

[38] S. A. Lekas, Closed-loop control of electromagnetic properties for 3d-printed graded refractive index lenses, MPhil thesis, University of Oxford (2022).

[39] L. Fieber, S. S. Bukhari, Y. Wu, P. S. Grant, In-line measurement of the dielectric permittivity of materials during additive manufacturing and 3D data reconstruction, Additive Manufacturing 32 (2020) 101010.

[40] L. Fieber, A hybrid additive manufacturing framework for the multi-phase fabrication and in-line characterization of functional devices, DPhil thesis, University of Oxford (2020).

[41] S. Lekas, R. Drummond, P. S. Grant, S. R. Duncan, Closed-loop control of dielectric permittivity for 3D-printed radio-frequency devices, in: Procs. of the IEEE Conference on Control Technology and Applications (CCTA), 2022, pp. 932–937.

[42] Avient, Preperm ABS500 (2022).

[43] A. Goulas, S. Zhang, D. A. Cadman, J. Järveläinen, V. Mylläri, W. G. Whittow, J. Y. C. Vardaxoglou, D. S. Engstrøm, The impact of 3D printing process parameters on the dielectric properties of high permittivity composites, Designs 3 (4) (2019) 50.

[44] H. Taghavian, R. Drummond, M. Johansson, Pole-placement for non-overshooting reference tracking, in: Procs. of the Conference on Decision and Control (CDC), IEEE, 2021, pp. 414–421.

[45] S.-H. Kim, Analytic solution of the generalized eaton lens, Journal of Modern Optics 68 (3) (2021) 143–145.

[46] Y. Zhao, M. Yong-Liang Zhang, X. Zheng, X. D. Dong, Z. Zhen-Sheng, Three-dimensional luneburg lens at optical frequencies, Laser & Photonics Reviews 10 (3) (2016) 665–672.